IEEE Access
Multidisciplinary ⋮ Rapid Review ⋮ Open Access Journal

Received 27 March 2025, accepted 16 April 2025, date of publication 21 April 2025, date of current version 29 April 2025.

Digital Object Identifier 10.1109/ACCESS.2025.3562632

RESEARCH ARTICLE

Reduced Inter-Element Interference mmWave MIMO Antenna and Its Application in WBAN

JAWAD AHMAD, (Graduate Student Member, IEEE), AND MOHAMMAD HASHMI, (Senior Member, IEEE)

Department of Electrical and Computer Engineering, School of Engineering and Digital Sciences, Nazarbayev University, 010000 Astana, Kazakhstan

Corresponding author: Mohammad Hashmi (mohammad.hashmi@nu.edu.kz)

This work was supported in part by the Science Committee of the Ministry of Science and Higher Education of the Republic of Kazakhstan under Grant AP19677597, and in part by Nazarbayev University Collaborative Research Program under Grant 111024CRP2018.

ABSTRACT Multi-input multi-output (MIMO) antennas operating in the millimeter wave (mmWave) band face challenges related to inter-element interference, limited isolation due to close spacing, and mutual coupling, all of which degrade antenna performance. To address these, this study introduces an advanced technique for enhancing inter-element isolation and minimizing mutual coupling. The proposed approach employs a combination of defective ground structures (DGS) and frequency-selective surfaces (FSS) to achieve effective isolation enhancement. Initially, a mmWave dual-band antenna was designed by incorporating a modified elliptical patch with rotating arms. Subsequently, a six-element dual-band MIMO antenna, measuring $1.97 \times 3.39\lambda^2$, was developed to operate in the 23.63–32.90 GHz and 36.68–40 GHz bands, covering both ISM and 5G NR bands. The proposed inter-element isolation technique successfully achieves a coupling reduction of 33 dB between the MIMO elements. Furthermore, the designed dual-band MIMO antenna maintains a broadside radiation pattern, with maximum realized gains of 9.12 dBi, 9.19 dBi, 8.80 dBi, and 8.77 dBi at 26 GHz, 28 GHz, 30 GHz, and 38 GHz, respectively. It also demonstrates excellent MIMO diversity performance, including a total active reflection coefficient of < -10 dB, an envelope correlation coefficient of <0.04, and a diversity gain of >9.91 dB. A specific absorption rate (SAR) analysis confirmed that the design complies with safety standards for both 1g and 10g tissue models. Additionally, a communication link scenario for wireless body area network (WBAN) applications was investigated. The combination of high isolation, dual-band functionality, broadside radiation, excellent diversity performance, and acceptable link margin validates the suitability of the proposed MIMO antenna for WBAN communication applications.

INDEX TERMS Antenna, dual-band, frequency-selective surface, mmWave, MIMO.

I. INTRODUCTION

THE fifth generation (5G) technology has significantly transformed Internet of Things (IoT) systems [1], [2], [3], [4], [5], [6], [7], [8]. Within the 5G regime, the sub-6 GHz band (called FR1) offers wide coverage, whereas the millimeter wave (mmWave) band (called FR2) provides significant bandwidth and higher data rates [9], [10]. Despite the considerable benefits of the mmWave band, it is beset with numerous challenges such as susceptibility to path losses and blockages which results in poor signal quality and range [11], [12], [13]. The use of multi-input-multi-output (MIMO) antennas can address this concern as they improve diversity, miniaturization, and intelligent features [14], [15], [16]. However, mmWave MIMO antennas suffer from increased mutual coupling and distorted radiation patterns owing to the miniature size of antenna elements and close spacings [17]. Existing MIMO antenna design techniques are impractical for applications like IoT, which rely on compactness and multi-band antenna operation [18].

Increasing the distance between MIMO antenna components can reduce mutual coupling but at the cost of a

The associate editor coordinating the review of this manuscript and approving it for publication was Lei Zhao.

significant increase in size. Therefore, various decoupling techniques have been employed to minimize mutual coupling and enhance isolation while keeping compactness. For example, at lower frequencies, the use of dielectric blocks [19], graded-index all-dielectric lenses [20], gradient relative permittivity superstrates [21], combining stubs with patches [22], and phase-shifting techniques [23] provide isolation of up to 20 dB. Furthermore, the L-shaped slot introduced in a flexible four-element MIMO antenna showed a low gain of 4.3 dBi and an efficiency of 0.70 for sub-6 GHZ frequencies [24]. Similarly, a wall of split-ring resonators between the E and H planes reduced mutual coupling at 10 GHz with 22 dB isolation but with added complexity [25]. The use of a dual-decoupling framework based on the defective ground structure (DGS) improved the isolation from 6 dB to over 20 dB for wideband microstrip patch antennas at frequencies below 10 GHz [26]. However, generally, these approaches have not been reported for mmWave MIMO antennas possibly due to increased complexities.

For mmWave frequencies, the use of parasitic shapes to reduce mutual coupling of a 4-element MIMO antenna has been reported in the literature [27]. Moreover, the incorporation of parasitic stubs near dipole patches reduced coupling between MIMO elements up to 17dB within the band of 28.5-35.3 GHz [28]. Another report provides an interesting scheme that makes use of parasitic stubs attached to electric dipole patches to achieve less than 22 dB coupling across 25.1-33.3 GHz by adjusting stub lengths [29]. Some recent reports include a wideband decoupling configuration confined electromagnetic fields along the array aperture achieving over 25dB isolation within 24.3-29.7 GHz [30], and current cancellation models for frequencies of 25.5–26.5 GHz [31].

However, it is important to note that while existing decoupling techniques are effective, they are primarily optimized for lower mmWave bands (e.g., n257) and often introduce increased complexity and cost [19], [20], [21], [22], [23], [25], [27], [29], [31]. To overcome these challenges, we propose a hybrid decoupling approach that integrates DGS and a metamaterial-based frequency-selective surface (FSS). The DGS introduces a high-impedance surface, effectively suppressing surface current interactions in the ground plane, while the FSS acts as a band-stop filter, preventing unwanted frequency components from propagating between elements. Unlike previous works [25], [26], [27], [28], [29], [30], [31] that rely on single-method decoupling, our proposed hybrid technique achieves exceptional isolation of >33 dB, while maintaining compact antenna size and high radiation efficiency.

It is noteworthy that the FSS on the top surface of the antenna, along with the integration of FSS and DGS in the ground plane, makes the proposed design a hybrid approach, combining both high-impedance and filtering characteristics to achieve a unique and effective decoupling mechanism. Moreover, this design is optimized for dual-band operation, covering both the ISM and n257/n258 5G NR mmWave bands, making the proposed antenna highly versatile. This ensures that the antenna can efficiently operate at multiple frequencies independently, eliminating the need for additional antennas for different frequency bands.

The key features and contributions of this work are summarized as follows:

1) Dual-Band Operation: Provides coverage for dual frequency bands and eliminates the necessity of incorporating multiple antennas to accommodate various frequencies. It efficiently operates across the 24–24.25 GHz ISM band, and FR2 band (n257, n258, and n260 sub-bands). The ISM band and any of the sub-bands can be simultaneously used.
2) High Isolation and Gain: The proposed novel hybrid DGS and FSS-based technique enables high isolation between inter-element ports, with coupling over >33 dB in the bands of interest. It also demonstrates high gain, with maximum realized gains of 9.12 dBi, 9.19 dBi, 8.80 dBi, and 8.77 dBi at 26 GHz, 28 GHz, 30 GHz, and 38 GHz, respectively. In addition, the proposed design achieves more than 0.90 efficiency in the entire impedance bandwidth.
3) Application: Communication and link margin scenarios in wireless body area networks (WBAN) within an IoT environment are investigated.
4) Cost: The design can be prototyped on a single substrate and hence does not require any additional manufacturing complexities making it very cost-effective.
5) Analysis: The characteristic mode analysis (CMA) to investigate the behavior of each stage to finalize the required bands allows systematic analysis and design.

This paper is divided into multiple sections. Section II focuses on the geometric design and CMA, whereas Section III explains the step-by-step process of designing mmWave MIMO antenna and the proposed hybrid decoupling technique for enhanced isolation. Section IV examines and discusses the measurement results, and Section V presents the calculation of MIMO antenna diversity parameters. Section VI describes the application of the proposed mmWave MIMO antenna and the communication link analysis, and Section VII concludes the paper.

II. SINGLE ELEMENT ANTENNA DESIGN

The single element antenna was designed using a four-step development approach, as illustrated in Fig. 1. The antenna was designed on a semi-flexible Rogers RT 5880 substrate (dielectric constant $=$ 2.2, copper thickness $=$ 0.017 mm, loss tangent $=$ 0.0009) and uses a full ground plane. The substrate dimensions were 16 mm $\times$ 16 mm $\times$ 0.79 mm^3. CST Microwave Studio was utilized for the simulations, and each design phase was thoroughly analyzed using CMA to optimize the desired impedance bandwidth. The antenna design began with a basic elliptical patch fed by a microstrip

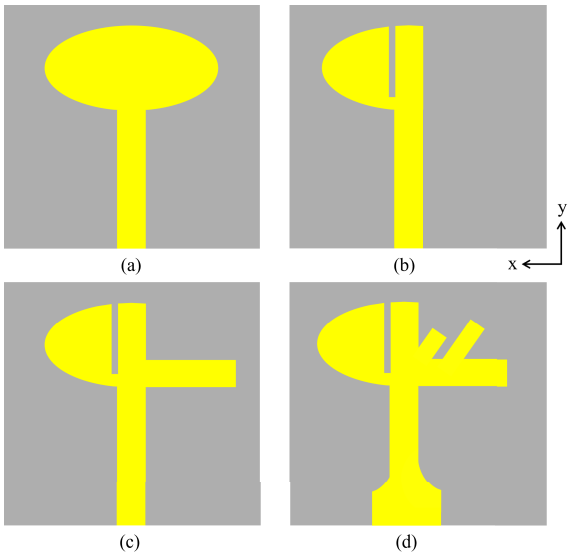

FIGURE 1. Development stages of single element antenna (a) stage 1, (b) stage 2,(c) stage 3, and (d) stage 4.

TABLE 1. Summary of modes behavior when MS = 1.

Type	λ_n	α_n	Behavior
Efficient	0	180°	Minimal energy storage, maximum radiation
Capacitive	< 0	$180° < \alpha_n < 270°$	Stores electric field energy, overexcited radiation
Inductive	> 0	$90° < \alpha_n < 180°$	Stores magnetic field energy, underexcited radiation

line, which served as the fundamental structure in Stage 1. In Stage 2, the elliptical patch was bisected, and an additional incision was made to shift the resonant frequency and optimize the impedance bandwidth. Stage 3 introduced an extended arm to further expand the bandwidth and improve radiation characteristics. Finally, in Stage 4, two rotating arms were added to achieve the desired dual-band operation, covering both the ISM and the 5G NR bands. Each of these stages are discussed in details in the following sub-sections.

A. CMA AND ALL DESIGN STAGES ANALYSIS

CMA facilitates the evaluation of the surface current of antenna structure by determining its eigenvalue (λ_n) and the corresponding current (J_n). CMA is an effective tool for antenna design because it predicts the radiation behavior of an antenna structure by analyzing the surface current without requiring any external excitation [32]. The CMA theory posits that random bodies, through orthogonal characteristic modal currents and weighted eigenvalues, can facilitate the support of multiple characteristic modes, as can be deduced from (1). Here, $[R, X]$ represents the real and imaginary parts of the impedance operator $Z(J_n)$ given in (2). The term $X(J_n)$ represents the characteristic modes associated with the energy storage. To ensure the dominance of these modes, it is crucial to minimize $X(J_n)$ to zero, thereby making

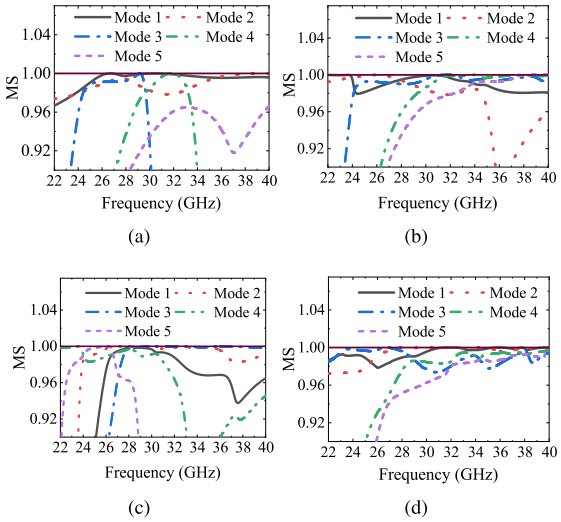

FIGURE 2. MS results (a) stage 1, (b) stage 2, (c) stage 3, and (d) stage 4.

the impedance real. This can be achieved by modifying the current pattern in the different regions of the designed structure by incorporating slots. The imaginary surface current $X(J_n)$ can be determined from the characteristic angle (α_n), which is a function of λ_n described in (3). The summation of all surface or characteristic currents is represented by (J), as shown in (4). The modal significance (MS) can then be calculated by utilizing weighted λ_n as specified in (5) [33], [34].

$$XJ_n = \lambda_n R J_n \tag{1}$$

$$Z(J_n) = R(J_n) + jX(J_n) \tag{2}$$

$$\alpha_n = 180° - \tan^{-1}(\lambda_n) \tag{3}$$

$$J = \sum_{n=1}^{\infty} \lambda_n \alpha_n \tag{4}$$

$$MS = \frac{1}{1 + j\lambda_n} \tag{5}$$

A MS value of 1 indicates the dominant resonant modes within the structure. However, not all modes of the structures exhibit resonance, as some will be capacitive and others inductive, as summarized in Table 1.

CMA analysis was used to evaluate each stage of the design process, ensuring that the final structure met the required bandwidth specifications. The CST Studio's eigenmode solver was used to examine the initial five modes. As a case study, the MS for all stages is shown in Fig. 2. Through independent analysis of the reflection coefficient for each stage in the frequency-domain solver, the dominant modes were effectively identified, and the results are presented in Fig. 3. For the stage 1 design, the CMA analysis was conducted at 28 GHz, and the MS results are shown in Fig. 2(a). The results reveal that the first four modes are significant, with their MS values approaching 1 at different frequencies. Specifically, Mode 1 exhibits a high MS almost

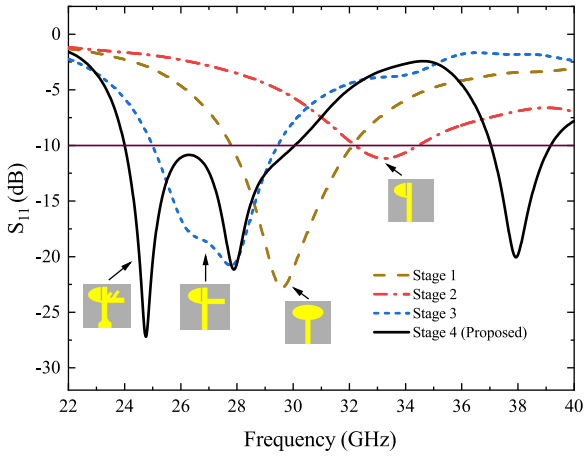

FIGURE 3. Comparison of the reflection coefficients of all stages.

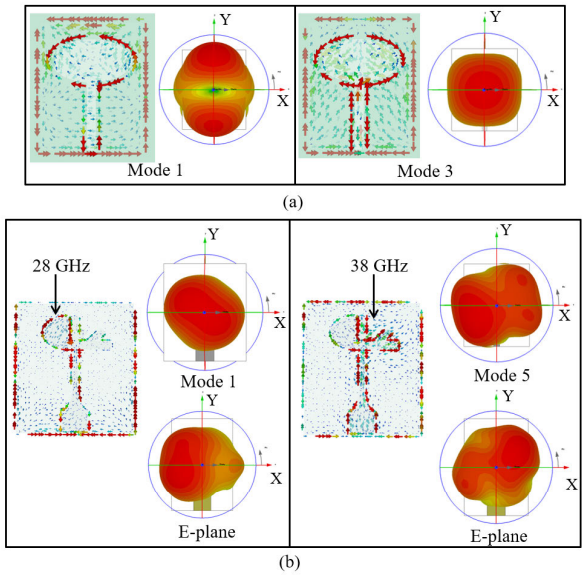

FIGURE 4. Surface current distribution and radiation patterns (a) stage 1 and (b) stage 4.

at all frequencies, Mode 2 shows significance near 38 GHz, Mode 3 peaks at 29 GHz, and Mode 4 reaches its maximum MS at 31.7 GHz. In contrast, Mode 5 does not converge to a significant value across the analyzed frequency range. The reflection results in Fig. 3 indicate that the stage 1 antenna impedance bandwidth extends from 27.89 GHz to 31 GHz. These resonant frequencies are predominantly influenced by modes 1 and 3, owing to their substantial MS values in proximity to the bandwidth, while other modes demonstrated less significant impact.

The stage 1 antenna operates in a single band primarily covering 30 GHz. However, the objective is to develop a dual-band antenna supporting multiple communication standards. Therefore, in the second stage, the ellipse was bisected along its center and an additional incision was made while maintaining the width of the transmission line. The

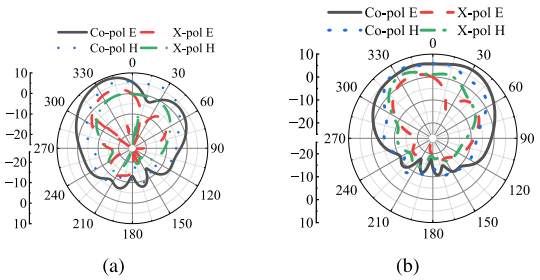

FIGURE 5. Single element antenna Co and X polarization at (a) 28 GHz and (b) 38 GHz.

MS results of stage 2 in Fig. 2(b) indicate that modes 1, 2, and 3 are the primary radiating mode as MS maintains its value near 1 over a wide frequency range. In contrast, modes 4 and 5 display lower MS values in desired bandwidth. The first three dominant mode combined contributions are also evident from the reflection coefficient in Fig. 3 that this design has an impedance bandwidth of 2 GHz covering 32-34 GHz frequencies. This stage provided a bandwidth shift but did not achieve the desired dual-band operation across the 24 GHz ISM band and the Ka-band. To further expand the bandwidth an additional stripline was introduced along the x-direction in stage 3 with the same width as the transmission line. The MS result of stage 3 design in Fig. 2(c) shows that Mode 1 remains the dominant radiating mode, with an MS value near 1 across a wide frequency range from 24 GHz to 30 GHz. Additionally, Mode 2 and Mode 3 exhibit a peak near 28 GHz and remain almost 1 at all frequencies. In contrast, Modes 4, and 5 have high MS values near 26 GHz and 28 GHz. The reflection coefficient results for stage 3, as shown in Fig. 3, indicate an impedance bandwidth of approximately 4.5 GHz, covering the 25-29.5 GHz range. This suggests that the majority of modes are constructively contributing within this frequency range, while their contribution outside this range remains minimal. This stage provided improved coverage at lower mmWave frequencies compared to stage 2 but still did not achieve the desired dual-band operation across both the 24 GHz ISM band and the Ka-band. Consequently, additional structural adjustments were performed in stage 4 to effectively meet the target frequency bands. Two arm structures were introduced in stage 4 and positioned along the extended microstrip line in the x-direction. The transmission line width was further adjusted to achieve the desired frequency bands. As depicted in Fig. 2(d), Modes 2 and 3 exhibit significant contributions near 28 GHz, while Mode 1 becomes dominant above 30 GHz. Additionally, Modes 4 and 5 show noticeable contributions from 33 GHz and 36 GHz onward. The reflection coefficient results in Fig. 3 indicate that the stage 4 design successfully achieves dual-band, covering both the 24-30 GHz and 37-39 GHz mmWave band. This implies that Modes 1 to 3 primarily contribute to the lower band whereas Modes 4 and 5 are effective for the upper band.

B. EM AND CIRCUIT MODELING ANALYSIS

1) RADIATION PATTERNS ANALYSIS

To highlight the impact of different modes on antenna performance, the surface current distribution and radiation patterns for the dominant modes of stages 1 and 4 are shown in Fig. 4. In stage 1, Mode 1 exhibits an in-phase surface current flow along the top edge of the elliptical patch and ground plane, with anti-phase currents at the outer left and right edges, resulting in a broadside radiation pattern that efficiently radiates energy in the z-direction, as shown in Fig. 4(a). Mode 3 follows a similar current distribution but with more localized and asymmetric currents, leading to a more directive broadside radiation pattern. For the stage 4 design, Fig. 4(b) shows that at 28 GHz, the current is concentrated along the half-elliptical patch in phase with the ground current, while at 38 GHz, the current is concentrated in the arm structures. Both configurations produce broadside radiation patterns. To validate the results, the radiation pattern of Mode 1 is compared with the simulated E-plane pattern at 28 GHz for stage 4, and the Mode 5 pattern is compared with the simulated E-plane pattern at 38 GHz. The good agreement between the simulated and CMA-derived patterns demonstrates the effectiveness of CMA in enhancing antenna bandwidth and radiation performance.

The 2D co-polarization (Co-pol) and cross-polarization (X-pol) radiation patterns of the single element antenna for both the E and H-planes are provided in Fig. 5. At 28 GHz, as shown in Fig. 5(a), the Co-pol patterns demonstrate a stable broadside radiation characteristic, while the X-pol levels remain moderate but become noticeable in specific angular directions, particularly in the backlobes and sidelobes. Similarly, at 38 GHz, as depicted in Fig. 5(b), a broadside Co-pol response is observed, with an increase in X-pol levels, especially in the backlobes and wide-angle directions. The 38 GHz band is achieved through the presence of the two arms in the antenna structure, as shown in Fig. 4. These arms are not symmetrical with the structure responsible for radiation at 28 GHz, leading to higher X-pol levels due to polarization leakage caused by structural asymmetries in the antenna design. Despite this, the X-pol levels remain below 0 dB, particularly in the main lobe direction, indicating that the overall polarization purity is acceptable for practical antenna applications.

2) PARAMETRIC ANALYSIS

The final stage 4 dual-band antenna variables are shown in Fig. 6, with the optimized parameter values (in mm) as follows: $S_W = 16.00$, $S_L = 16.00$, $W_1 = 0.70$, $W_2 = 3.00$, $W_3 = 0.70$, $W_4 = 0.95$, $A_1 = 1.05$, $A_2 = 1.58$, $A_L = 3.78$, $L_1 = 14.00$, $L_2 = 2.40$, $L_3 = 5.05$, $\theta = 130°$, $R_W = 3.71$, $R_C = 0.54$, $R_L = 3.40$. A parametric analysis was also conducted to evaluate the influence of critical parameters on the impedance bandwidth. As shown in Fig. 7(a), an increase in L_2 results in a reduction in both the magnitude and the overall impedance bandwidth. Conversely, Fig. 7(b) illustrates that W_3 has an inverse effect, primarily influencing the upper-frequency band. Increasing W_3 causes a leftward frequency shift within the band. The rotation of the arm structure also plays a role in shaping the bandwidth, as demonstrated in Fig. 7(c). The parameter R_C exhibits a comparable impact on the bandwidth, as shown in Fig. 7(d). The analysis indicates that the desired dual-band characteristics were achieved at $R_C = 0.54$ mm.

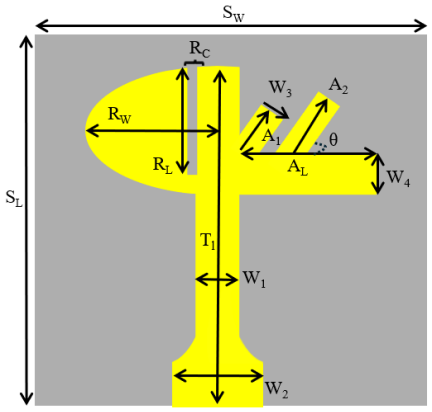

FIGURE 6. Final stage 4 antenna dimensions.

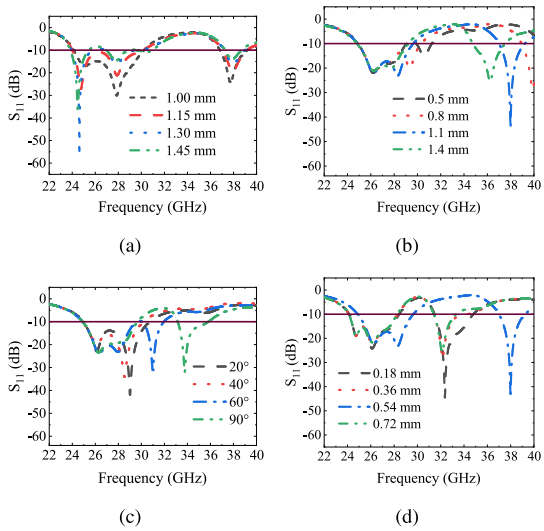

FIGURE 7. Parametric analysis (a) L_2, (b) W_3, (c) θ, and (d) R_C.

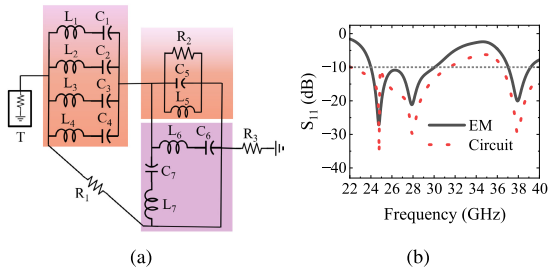

FIGURE 8. Single element antenna (a) RLC circuit model and (b) EM and RLC circuit based S_{11} comparison.

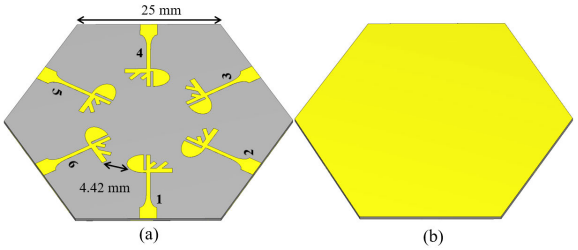

FIGURE 9. **MIMO$_1$ design (a) top and (b) bottom.**

3) RLC CIRCUIT MODEL ANALYSIS

The equivalent circuit model represents the antenna's electrical behavior using lumped components: resistor (R), inductor (L), and capacitor (C). The RLC circuit model of the single antenna element is shown in Fig. 8(a). Based on electromagnetic (EM) simulations in CST, it was determined that the antenna exhibits a dual-band response. To predict this behavior, a combination of series and parallel RLC circuits was optimally designed in ADS. In the circuit model, the first band (24–30 GHz) is represented by the RLC circuit highlighted in orange, while the second band (37–39 GHz) is represented by the RLC circuit highlighted in pink. The dual-band response (f_{0n}) of the RLC circuit are approximated as following.

$$f_{01} = \frac{1}{2\pi\sqrt{L_{eq1}C_{eq1}}} \tag{6}$$

$$f_{02} = \frac{1}{2\pi\sqrt{L_{eq2}C_{eq2}}} \tag{7}$$

where L_{eqn} and C_{eqn} are the equivalent inductance and capacitance of the circuits highlighted in orange and pink in Fig. 7(a). In the circuit, T denotes a 50 Ω terminator. The component values are as follows: : $L_1 = 1.75$, $L_2 = L_7 = 1.55$, $L_3 = 16.5$, $L_4 = L_6 = 1.62$, $L_5 = 16.5$ (nH), $C_1 = 0.02$, $C_2 = C_7 = 0.01$, $C_3 = 0.002$, $C_4 = C_6 = 0.02$, $C_5 = 0.002$ (pF), $R_1 = 130$, $R_2 = 1$, and $R_3 = 50.5$ Ω. The reflection coefficient results of the RLC circuit compared with the EM model are shown in Fig. 8(b). The RLC circuit model exhibits a broader bandwidth compared to the EM model, likely due to its simplified lumped-element approximation, which does not account for higher-order EM effects, material losses, and impedance variations. In contrast, the EM model considers surface waves and radiation losses, resulting in a more constrained bandwidth. Additionally, the idealized components in the RLC model do not fully capture frequency-dependent losses and parasitic effects present in the physical antenna, leading to an overestimation of bandwidth. Nevertheless, the designed RLC model closely follows the behaviour of the EM simulation model at the desired resonant frequencies.

III. DESIGN OF DUAL-BAND MIMO ANTENNA

The channel capacity (C) of a MIMO system with transmit (N_t) antennas is given in (8) [35].

$$C = \log_2 \det\left(I_N + \frac{\rho}{N_t} HH^H\right) \tag{8}$$

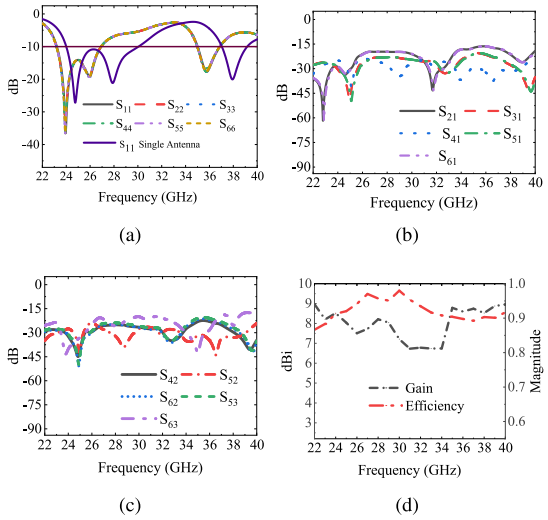

FIGURE 10. **Results of MIMO$_1$ (a) reflection coefficients, (b) and (c) transmission coefficients, and (d) gain and efficiency.**

where I_N is the identity matrix, ρ is the signal to noise ratio (SNR), and H is the channel matrix. One method to increase the capacity is to incorporate multiple antennas on both the transmitter and receiver sides. For wearable devices, particularly those used in WBANs, high data rates are often required to support applications such as real-time health monitoring. While increasing the number of antennas can enhance data rates, it also increases the overall size and complexity of the system, which may not be practical for WBAN due to space limitations. Therefore, there must be an optimum number of antenna elements that balances performance. In order to achieve higher capacity and data rates, the designed dual-band antenna has been transformed into a six-element MIMO configuration with a full ground plane (MIMO$_1$). Subsequently, a dual-band MIMO antenna with DGS(MIMO$_2$) is designed to improve the inter-element isolation. Finally, a hybrid DGS and FSS structure incorporated a dual-band MIMO antenna to further enhance inter-element isolation (MIMO$_3$). The six-element will provide a balance between performance and miniaturization. Compared to 2- or 4-element MIMO antenna, the proposed design will achieves higher capacity and diversity gain which are critical for WBAN applications. Furthermore, each of the antenna elements is arranged in a hexagonal configuration. The hexagonal MIMO layout is selected to ensure consistent broadside radiation characteristics while also enhancing pattern diversity through optimized element placement. In contrast to conventional linear or rectangular MIMO antennas, the hexagonal configuration maintains a stable broadside radiation pattern while minimizing pattern distortion and undesired side lobes [36], [37].

A. DESIGN OF MIMO$_1$

The MIMO$_1$ consists of six elements on a hexagon-shaped substrate as shown in Fig 9. The inter-element top

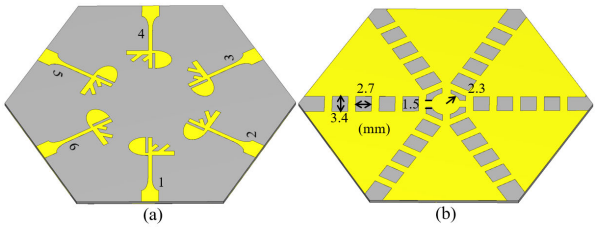

FIGURE 11. MIMO$_2$ design (a) top and (b) bottom.

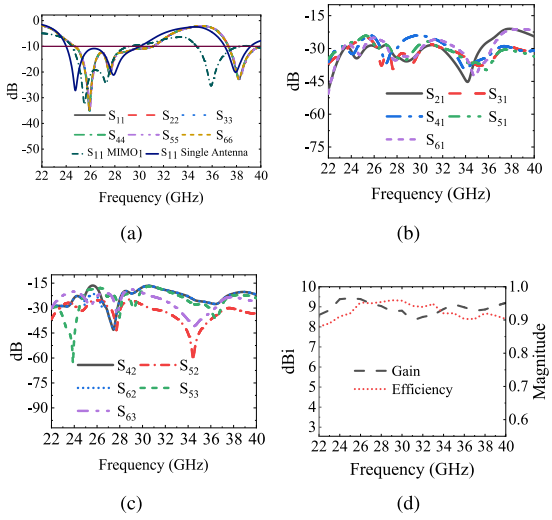

FIGURE 12. Results of MIMO$_2$ (a) reflection coefficients, (b) and (c) transmission coefficients, and (d) gain and efficiency.

edge-to-edge spacing is 4.42 mm which is less than half the wave spacing of all operating frequencies. The s-parameters, gain, and efficiency of the designed MIMO$_1$ are plotted in Fig. 10. It is apparent that the placement of single element antenna on a hexagonal substrate has shifted the impedance bandwidth. For instance, the lower band is shifted from 23.95-30.05 GHz to 23.18-26.89 GHz, and the upper band is shifted from 37.05-39.13 GHz to 34.97-36.85 GHz. This shift is both evident and inherent, as it arises from changes in the ground plane, which plays a critical role in determining the impedance characteristics of the antenna. The hexagonal shape of the substrate causes multiple edge terminations, which alter the current distribution. This, in turn, modifies the effective electrical length, leading to shifts in the resonance frequency. Furthermore, mutual coupling also impacts the bandwidth. However, this bandwidth shift was effectively optimized in the final proposed MIMO antenna design. In this MIMO$_1$ design, as shown in Figs. 10(b-c), the coupling levels between all six elements were observed to be below 20 dB. Additionally, as shown in Fig. 10(d), gain is now more than 7.50 dBi and radiation efficiency greater than 0.90 across the entire impedance bandwidth.

B. DESIGN OF MIMO$_2$

To further enhance isolation and address the shift in bandwidth, DGS in the forms of slots is incorporated in the ground plane as illustrated in Fig. 11. The slots were introduced which covers the inter-element spacing in both x- and y- planes. This results in the bandwidth increase which now covers 24.61–31.61 GHz in the lower frequency band and 37.30–40.05 GHz in the upper band, encompassing all desired 26 GHz, 28 GHz, 30 GHz, and 38/39 GHz frequency bands, as shown in Fig. 12(a). Although high isolation ($>$ 20 dB) is observed, particularly between port 1 and all other elements, as shown in Fig. 12(b), the level of isolation is higher in elements that are face-to-face, i.e., S_{42}, S_{62}, S_{53}, and S_{63}, as shown in Fig. 12(c). Moreover, as depicted in Fig. 12(d), the incorporation of slots increased the gain to exceed 8.50 dBi, with an radiation efficiency greater than 0.90 observed across the entire impedance bandwidth.

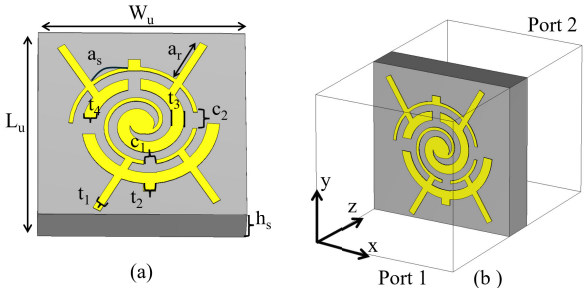

FIGURE 13. FSS design (a) unit cell and (b) floquet boundaries.

C. THE FINAL PROPOSED HYBRID DESIGN: MIMO$_3$

1) FSS DESIGN

The FSS consists of patterned metallic surfaces, where its dimensions, configuration, and spacing has a crucial role in determining the filtering characteristics. By exhibiting a band stop behavior, the FSS has the potential to effectively block or attenuate the surface waves between antenna elements. It will then lead to enhanced isolation and minimized interference between the MIMO antenna elements. The FSS unit cell in this work is a modified variant of the spiral-shaped resonator that is designed on the same Rogers RT5880 substrate with dimensions of 3.52 $\times$ 3.52 mm. The upper surface of the FSS comprises two spiral-shaped concentric metallic rings, wherein cuts are introduced to generate capacitance while the rings provide inductance. The metallic rings were then joined by four arms starting from the thicker ring, as shown in Fig. 13(a). Notably, the FSS design does not incorporate a ground plane. The optimized parameters of the FSS unit cell are as follows: $L_U = 3.52$, $W_U = 3.52$, $t_1 = 0.14$, $t_2 = t_3 = c_1 = c_1 = 0.21$, $a_s = 0.68$, $a_r = 0.68$, $a_r = 0.61$, $t_4 = 0.07$, $g_r = 0.16$, $g_r = 0.14$, and $h_s = 0.79$ (mm). The simulation of the unit cell was performed using Floquet boundary conditions with Ports 1 and 2. In this setup shown in Fig. 13(b), Port 1 is excited to transmit a standard plane wave in the z-direction, which is then received by Port 2. The incoming plane waves interacts with the metallic rings of the unit cell, resulting in bandpass and bandstop characteristics. The objective is to achieve

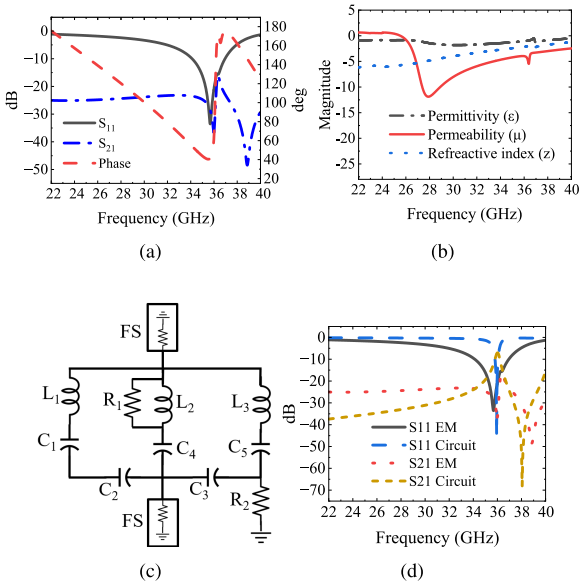

FIGURE 14. FSS unit cell (a) s-parameters, (b) effective parameters, (c) RLC circuit, and (d) comparison result of EM and circuit based models.

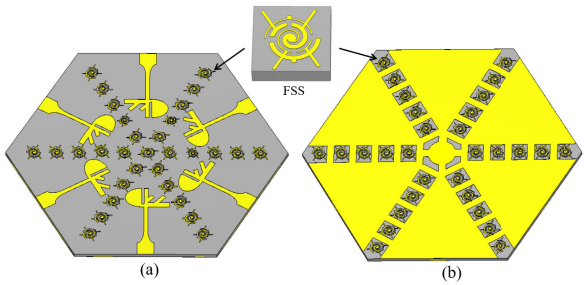

FIGURE 15. MIMO$_3$ design (a) top and (b) bottom.

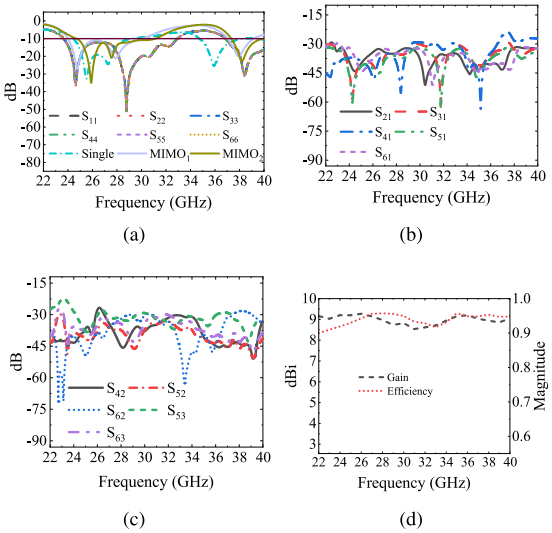

FIGURE 16. Results of MIMO$_3$ (a) reflection coefficients, (b) and (c) transmission coefficients, and (d) gain and efficiency.

broadband or dual-band suppression that effectively covers the primary resonant frequencies of the MIMO antenna.

The designed FSS unit cell exhibits both frequency-selective filtering and metamaterial characteristics. The results in Fig. 14(a) demonstrate a reflection of more than -5 dB and a transmission of less than -23 dB up to 35.6 GHz, along with transmission suppression of -30 dB or lower beyond 37 GHz. This behavior confirms the band-reject characteristics of the structure. Additionally, between 34 GHz and 36 GHz, the unit cell exhibits a bandpass response. The band-reject characteristic is crucial because when the MIMO antenna operates at its resonant band, it generates surface currents at these frequencies, which can induce mutual coupling in adjacent antennas. By integrating a band-reject response between MIMO antenna elements, these surface wave interactions can be significantly suppressed, thereby reducing mutual coupling. Furthermore, Fig. 14(b) demonstrates that the unit cell exhibits metamaterial-like properties, including negative permittivity (ε), permeability (μ), and refractive index (z). Unlike conventional FSS structures that primarily function as passive frequency filters, the proposed design also modifies electromagnetic wave propagation through engineered effective medium parameters. These parameters were derived using the Kramers-Kronig algorithm [38].

The RLC equivalent circuit model of the designed unit cell is shown in Fig. 14(c). The RLC circuit collectively emulate the distributed reactive and resistive characteristics of the FSS structure. The inductive components (L_1, L_2, L_3) represent magnetic energy storage in terms of the conductive paths and current loops within the resonator. The capacitive elements (C_1, C_2, C_3, C_4, C_5) correspond to the gaps and coupling effects between adjacent metallic regions and the storage of electric energy. Similarly, the resistors (R_1, R_2) represents the conductor, dielectric, and radiation losses in FSS structure. The performance of the RLC circuit model closely aligns with EM simulations, as evidenced by the s-parameters comparison in Fig. 14(d). The strong agreement between the circuit-based and EM-simulated S_{11} and S_{21} responses validates the accuracy of the equivalent circuit in predicting the frequency-selective behavior of the FSS. Some minor deviations exists between the circuit model and EM results that can be attributed arise to EM interactions which are not fully captured by the lumped-element representation. Nevertheless, incorporating both series and parallel LC resonances, the RLC model successfully replicated the dual-band behavior. The FSS circuit was optimized in ADS and the final values are: FS is free space impedance of 377 Ω, L_1, 192.1, $L_2 = 411$, $L_3 = 190.18$ (nH), $C_1 = 0.080$, $C_4 = 0.102$ (fF), $C_2 = 0.92$, $C_3 = 1.01$, $C_4 = 0.0001$ (pF), $R_1 = 1$K and $R_2 = 150$ (Ω).

D. DESIGN OF MIMO$_3$

The designed FSS was placed between the antenna elements on the top face and in the ground plane, as shown in Fig. 15. The distance between each FSS structure was precisely fixed at 1.4 mm. It is evident from the results in Fig. 16(a) that

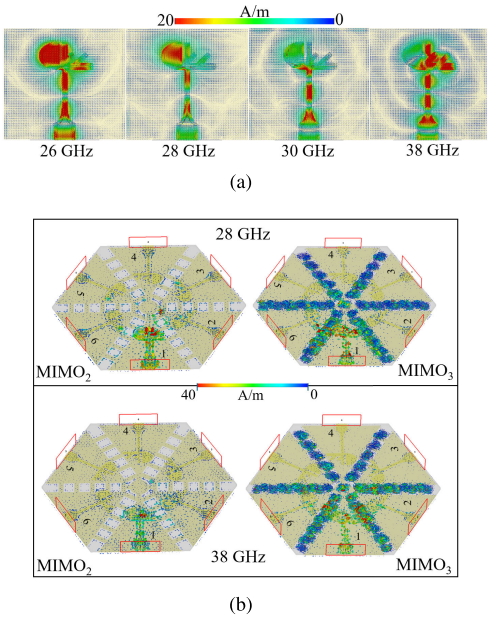

FIGURE 17. Surface current distribution: (a) single antenna element, (b) distribution in $MIMO_2$ and $MIMO_3$ (left).

the incorporation of FSS enhances the impedance bandwidth. The lower impedance bandwidth spans now from 23.63 GHz to 32.90 GHz, while the upper band extends from 36.68 GHz to over 40 GHz. Additionally, the inter-element isolation significantly improves with over 33 dBi of isolation observed at all resonant frequencies in all elements, except for the S_{41} and S_{42} elements, where -23 dBi isolation is obtained as can be seen in Figs. 16(b-c). Furthermore, the integration of the FSS results in increased gain of 8.90 dBi and more than 0.92 radiation efficiency throughout the impedance bandwidth and is given in Fig. 14(d). The enhanced isolation and reduction in mutual coupling show the effectiveness of the proposed mutual coupling reduction approach.

E. SURFACE CURRENT DISTRIBUTION

The results of surface current distributions, both for single antenna element and MIMO designs ($MIMO_2$, and $MIMO_3$) are presented in Fig. 17. The behavior of a single element antenna at frequencies of 26 GHz, 28 GHz, 30 GHz, and 38 GHz is shown in Fig. 17(a). The results show that the surface current concentrations occur in the half-elliptical region at 26 GHz and 28 GHz, indicating the origin of the resonance. Similarly, at 30 GHz, the current is more concentrated in the transmission line and part of elliptical shape, while at 38 GHz, it is more prominent in the rotating arms region. The reduction in mutal coupling is evident from the surface current distribution particularly in final $MIMO_3$ design as shown in Fig. 17(b). It is imperative to note that this distribution was achieved when port 1 was active, with all other ports were matched with 50 Ω. As expected, the surface current density is notably higher in the absence of the FSS, contributing to increased mutual coupling between

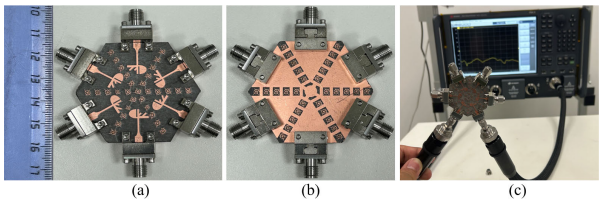

FIGURE 18. Fabricated prototype (a) top face, (b) bottom face, and (c) s-parameters measurements using VNA.

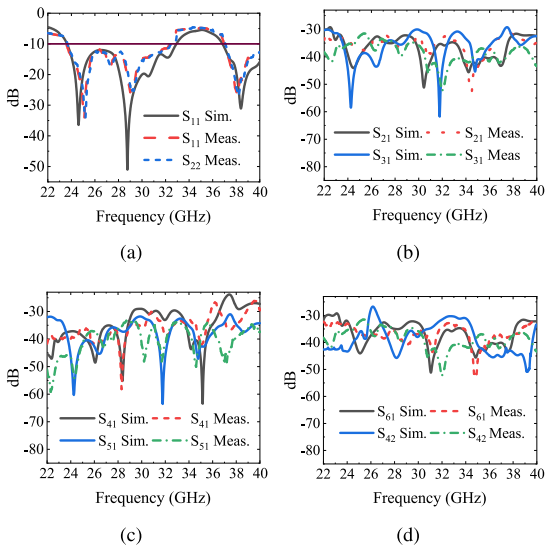

FIGURE 19. Comparison of simulation and measurement results: (a) reflection coefficients, and (b), (c) and (d) transmission coefficients.

antenna elements. However, the introduction of the FSS between the antenna elements significantly reduces the surface current interaction, with the current becoming more concentrated around the FSS structures. This demonstrates the effectiveness of the proposed FSS in suppressing unwanted coupling and improving isolation. The results reveal that although DGS can enhance isolation, but the FSS in conjunction with DGS exhibits superior inter-element decoupling due to its band stop behavior, which effectively blocks surface wave propagation between adjacent antenna elements.

IV. MEASURED RESULTS AND DISCUSSIONS

For the analysis of the measurement results, the $MIMO_3$ design was fabricated, and a prototype and measurement setup were developed using a Keysight network analyzer (PNA-X, N5247B) as shown in Fig. 18(a-c). The s-parameters simulation and measured results comparison are shown in Fig. 19. As shown in Fig. 19(a), the measurement results for the first two antenna elements follow the trends of the simulation data, although slight variations can be observed owing to fabrication restrictions. In this case, the measured impedance bandwidth was 23.65 GHz to 32.51 GHz, while the other had a bandwidth of 37.1 GHz and more than 40 GHz, which is practically the same

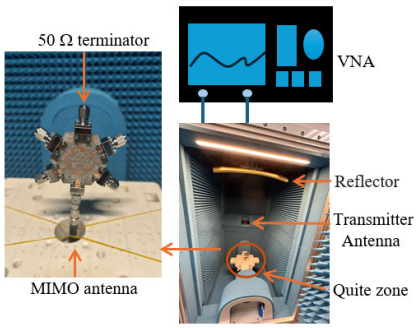

FIGURE 20. MIMO antenna gain measurements in the anechoic chamber.

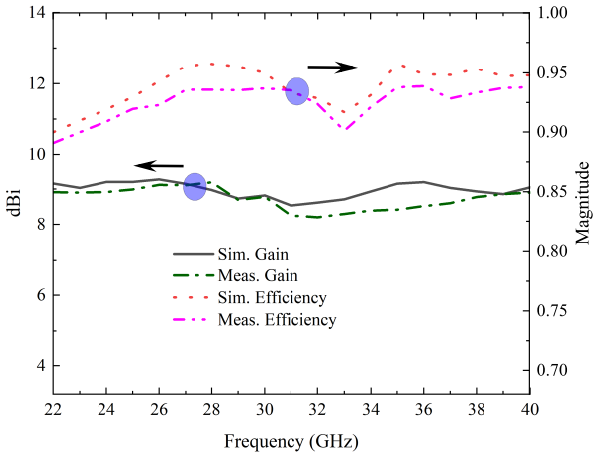

FIGURE 21. Simulated and measured gain and radiation efficiency of the MIMO antenna.

as the simulation results. It should be noted that when measuring the results, the other ports were terminated with 50 Ω terminators, and similar results were obtained for all ports. Measurements also validated the substantial isolation between neighboring ports, with results compared to simulations shown in Figs. 19(b–d). The measured coupling remained below 33 dB for the majority of the frequency range of interest, demonstrating the efficacy of the integrated DGS and FSS structures in reducing mutual coupling. This indicates that the radiation energy between adjacent element pairs is significantly attenuated.

The gain measurements were conducted in the Rhodes & Schwarz RS® ATS1800C CATR (Compact Antenna Test Range) chamber. This advanced anechoic chamber is specifically designed for precise far-field antenna measurements within a compact space. It employs a parabolic reflector to transform the spherical wavefront generated by a transmitter antenna into a plane wave within the quiet zone, ensuring accurate far-field testing without the need for a large test distance. As illustrated in Fig. 20, the proposed $MIMO_3$ antenna under test (AUT) was positioned in the quiet zone, where the wavefront is uniform. A 50Ω terminator was connected to other ports to ensure impedance matching and minimize unwanted reflections. The measurement process

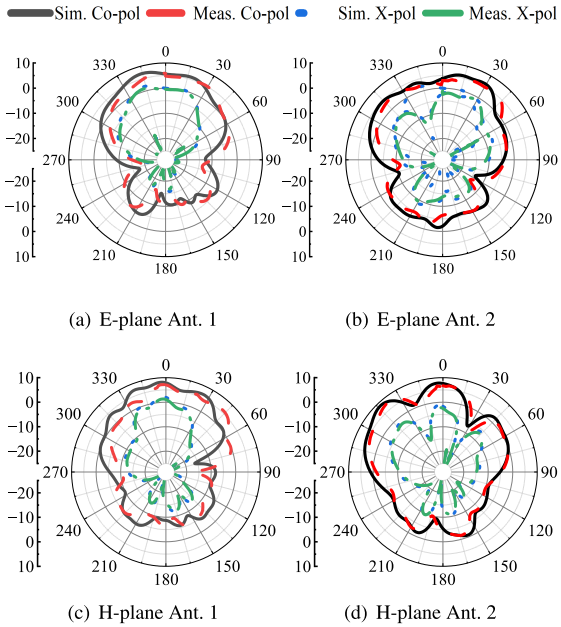

FIGURE 22. Comparison of E-plane radiation patterns at 28 GHz.

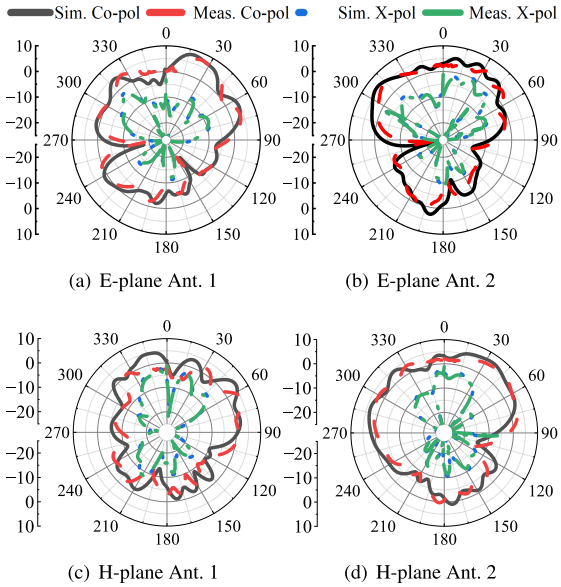

FIGURE 23. Comparison of H-plane radiation patterns at 38 GHz.

followed a systematic approach to ensure accuracy. Initially, the S_{11} parameter was measured using a VNA to verify impedance matching. A standard gain horn antenna with known gain G_{ref} was used as a reference to determine the gain of the AUT G_{AUT} using the gain transfer method (9) [39].

$$G_{\text{AUT}} = G_{\text{ref}} + 20\log\left(\frac{P_{\text{AUT}}}{P_{\text{ref}}}\right) \tag{9}$$

where P_{AUT} and P_{ref} represent the measured received power strengths of the AUT and the reference antenna, respectively.

Since directivity is a fundamental characteristic of an antenna's radiation pattern, it is typically obtained from

full-wave electromagnetic simulations. In this study, directivity values were extracted from the simulated far-field radiation pattern of the $MIMO_3$ antenna using CST. This ensures a fair comparison with the measured gain values. Since the gain of the AUT was measured using a calibrated VNA setup and in an anechoic chamber, the radiation efficiency was then measured as given in (10).

$$\eta_{\text{rad}} = \frac{G_{\text{AUT}}}{D_{\text{AUT}}} \tag{10}$$

The measured antenna gain and efficiency of the MIMO antenna are shown in Fig. 21. The measured results are in agreement with the simulation. The gain values for 26 GHz, 28 GHz, 30 GHz, and 38 GHz were 9.12 dBi, 9.19 dBi, 8.80 dBi, and 8.77 dBi. Similarly, the radiation efficiency values were 0.93 in most parts of the impedance bandwidths. The measurements of both Co-pol and X-pol components in the E-plane and H-plane at 28 GHz and 38 GHz were performed. As shown in Figs. 22 and 23, the proposed MIMO antenna demonstrates a broadside radiation pattern in both the E-plane and H-plane for all measured elements. This broadside characteristic is particularly crucial for wearable and off-body communication scenarios, as it ensures that the antenna radiates maximum energy away from the body. Furthermore, the X-pol levels in both planes remain well suppressed in the main beam direction, with the measured X-pol components significantly lower than the Co-pol components. While the X-pol levels increase at certain angles due to the asymmetrical structure of the antenna, they remain within acceptable limits. This behavior confirms the high polarization purity of the proposed MIMO antenna design and minimizes the risk of polarization mismatch in MIMO systems.

V. MIMO DIVERSITY ANALYSIS

A. TOTAL ACTIVE REFLECTION COEFFICIENT (TARC)

The TARC is a key metric used to evaluate the operational performance of a MIMO antenna across various input signal phase combinations. It is particularly useful for determining how well a MIMO antenna operates under active excitation conditions, where the input signals at different ports may have varying phases. It is calculated by comparing the total outgoing power (reflected power) at the antenna ports to the total incident power (input power) [40]. For a six-element MIMO antenna, TARC can be expressed as show in (11).

$$TARC = \sqrt{\frac{\sum_{i=1}^{6} |R_i|^2}{\sum_{i=1}^{6} |I_i|^2}} \tag{11}$$

where, $|R_i|$ and $|I_i|$ are the reflected and incident power, respectively. The TARC of the proposed MIMO antenna was evaluated for phase angles ranging from 0° to 180° in increments of 30° to assess its performance under varying excitation conditions. As shown in Fig. 24, the TARC exhibits distinct frequency-dependent behavior, with particularly strong performance observed at 28 GHz and 38 GHz, where

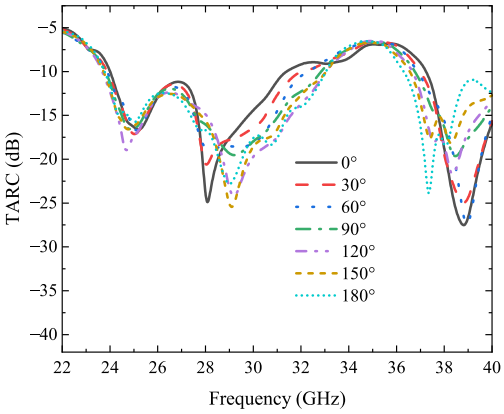

FIGURE 24. TARC of the MIMO antenna.

the TARC values are close to -30 dB. While phase-dependent variations are evident within the impedance bandwidth, the TARC consistently remains below the -10 dB threshold in both frequency bands. This demonstrates that the proposed MIMO antenna maintains excellent impedance matching and low reflection losses, even under varying excitation conditions. The low TARC values confirm that the antenna is well-decoupled in both frequency bands.

B. ENVELOPE CORRELATION COEFFICIENT (ECC), AND DIVERSITY GAIN (DG) ANALYSIS

The ECC shows the correlation between the radiation patterns of different antenna elements. It provides valuable insight into the ability of antenna elements to operate independently in a multipath environment. ECC values typically range between 0 and 1, where an ECC value of zero indicates complete isolation between the antenna elements, meaning there is no correlation between their radiation patterns. Conversely, an ECC value of 1 signifies complete correlation and poor diversity performance. In practical MIMO systems, an ECC value below 0.5 is generally considered sufficient to ensure adequate isolation and diversity. The ECC was calculated based on the far-field radiation patterns of the antenna elements using the expression 12 [41].

$$ECC(j,k) = \frac{\left(\int_0^{2\pi}\int_0^{\pi}\left\{X_{PR}.E_{\theta_j}E^*_{\theta_k}P_\theta + E_{\phi_j}E^*_{\phi_k}P_\phi\right\}d\Omega\right)^2}{\int_0^{2\pi}\int_0^{\pi}\left\{X_{PR}.E_{\theta_j}E^*_{\theta_j}P_\theta + E_{\phi_j}E^*_{\phi_j}P_\phi\right\}d\Omega} \times \int_0^{2\pi}\int_0^{\pi}\left\{X_{PR}.E_{\theta_k}E^*_{\theta_k}P_\theta + E_{\phi_k}E^*_{\phi_k}P_\phi\right\}d\Omega \tag{12}$$

Where:

- E_{θ_j} and E_{ϕ_j} are the far-field radiation patterns of the j-th antenna element in the θ- and ϕ- polarization, respectively.
- E_{θ_k} and E_{ϕ_k} are the far-field radiation patterns of the k-th antenna element in the θ- and ϕ- polarization, respectively.
- X_{PR} is the cross-polarization ratio.

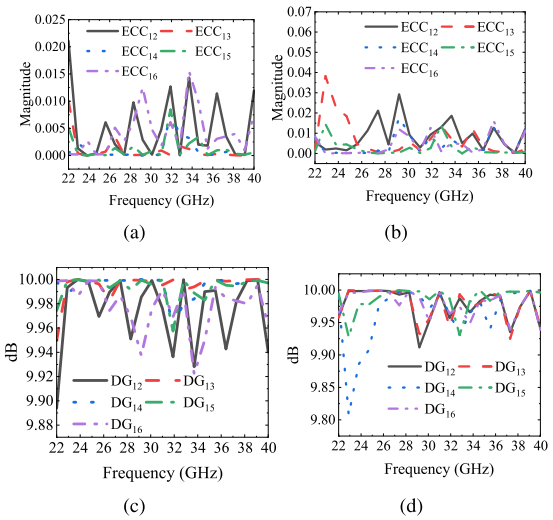

FIGURE 25. ECC and DG results (a) ECC far-field, (b) ECC Gaussian, (c) DG far-field, and (d) DG Gaussian.

- P_θ and P_ϕ are the power patterns in the θ- and ϕ-polarizations, respectively.

The ECC was evaluated for both far-field and realistic propagation scenarios, as shown in Fig. 25. The ECC measurements using the far-field model in Fig. 25(a) indicate that the ECC remains below 0.02 across the entire frequency band of interest, demonstrating excellent diversity performance.

To further validate the antenna's performance in real-world environments, the ECC was analyzed under a realistic propagation model that considers a Gaussian angular distribution in the elevation plane (θ) and a uniform angular distribution in the azimuth plane (ϕ) [42], [43]. Fig. 25(b) shows the ECC results for a mean elevation angle ($m_v = m_h$) of 45° and an angular spread ($\sigma_v = \sigma_h$) of 90° in both the vertical and horizontal planes. The evaluation reveals that, even under realistic propagation scenarios, the ECC values remain consistently below 0.04, which is well within the acceptable limit of 0.5 for MIMO systems. The DG was calculated for both far-field and realistic Gaussian distributions using (13) as following:

$$DG = 10\sqrt{1 - (\text{ECC})^2} \tag{13}$$

The ideal DG level for achieving optimal diversity performance in MIMO systems is 10 dB, which indicates minimal correlation between antenna elements and highly efficient signal decorrelation. In the context of the proposed dual-band MIMO antenna, the DG results exhibit consistently high values, showing its suitability for practical wireless applications. As shownin Fig. 25(c) for the far-field scenario and Fig. 25(d) for the realistic scenario, the DG remains above 9.91 dB across the entire impedance bandwidth. This demonstrates that the antenna sustains exceptional diversity performance under diverse propagation conditions. The high DG and low ECC across both far-field and realistic propagation environments confirm that the proposed MIMO antenna is effectively optimized for dual-band mmWave operation.

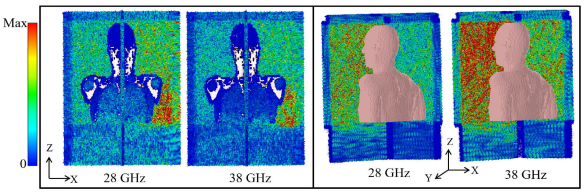

FIGURE 26. E-field distributions when MIMO antenna is placed on arm and chest regions.

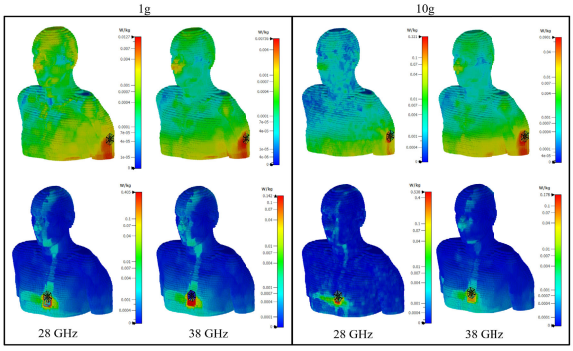

FIGURE 27. SAR values of 1g and 10g at the arm and chest regions.

TABLE 2. Peak SAR values for 1g and 10g at the arm and chest regions and at a power level of 500 mW.

Region	Frequency (GHz)	1g (W/kg)	10g (W/kg)
Arm	28	0.01227	0.0321
Arm	38	0.00736	0.00901
Chest	28	0.405	0.538
Chest	38	0.142	0.178

VI. MIMO ANTENNA APPLICATION SCENARIO

A. WBAN

WBAN communication consists of device-to-device (on-body) and device-to-off-body links. On-body communication typically requires omnidirectional or end-fire radiation patterns to maintain stable connections despite body movements, while off-body communication relies on broadside patterns to transmit data to external processing units or network infrastructure [44]. The measured results in Figs. 22 and 23 show that the proposed antenna exhibits broadside radiation patterns which can be an excellent candidate for effective off-body communication in WBANs. Furthermore, the 0.79 mm thickness of the substrate provides a semi-flexible structure that can conform to various parts of the human body, such as the arms or legs. Moreover, the proposed antenna's dual-band capability can enable reliable communication across different communication channels simultaneously. For instance, one frequency can be used for continuous data transmission to medical professionals, while another

can be allocated for receiving and implementing medical care instructions. Given its broadside radiation patterns, semi-flexible structure, and multi-frequency operation, the proposed antenna was selected as a case study for WBAN applications.

1) E-FIELD AND SAFETY ANALYSIS

The E-field distribution of the proposed antenna in WBAN applications can be utilized to evaluate its performance when positioned on the human body. This was analyzed with the antenna placed on the chest and arm of the CST Hugo voxel model at 28 GHz and 38 GHz, as shown in Fig. 26. The field distributions show that the antenna MIMO antenna E-field is away from the body in both cases, confirming a broadside radiation pattern. This outward-directed radiation shows the effectiveness of the proposed antenna in off-body communication scenarios in WBAN. The antenna was also evaluated for safety by calculating the SAR values at 28 GHz and 38 GHz as shown in Fig. 27 and summarized in Table 2. According to the guidelines set by the International Commission on Non-Ionizing Radiation Protection (ICNIRP) and the IEEE C95.1-2019 standard, the average SAR values for on-body applications must remain below 1.6 W/kg for 1 gram of tissue and 2.0 W/kg for 10 grams of tissue [45]. Although more SAR is present in the chest due to more proximity to the antenna, neverthe less all SAR values remain well below the international safety limits. These results confirm that the proposed MIMO antenna operates within the safety limits for on-body applications and thus is suitable for use in a WBAN environment. It should be noted that, to accelerate the simulation speed, the Hugo model was simplified by including only the skin, fat, and muscle layers. The MIMO antenna was positioned above this model at a distance of 2 mm. The tissue properties were then obtained from the IT'IS database [46] and selected according to the SAR calculations for each simulation frequency.

2) MEASUREMENTS ON HUMAN BODY

Measurements were conducted on human subjects, and the results were compared with those obtained from the CST Hugo voxel model. The antenna was positioned on both the chest and arm regions. Fig. 28 presents the corresponding reflection coefficient results. As demonstrated in Fig. 28(a), the bandwidth remained predominantly unchanged when the antenna was placed on the chest. However, Fig. 28(b) illustrates a slight decrease in bandwidth for the arm placement. This reduction can be attributed to the arm's more bent curvature compared to the chest. Furthermore, when the antenna was positioned on the human body, a significant shift in the reflection coefficient was observed due to impedance mismatch caused by tissue proximity and near-field coupling, resulting in the body absorbing energy. Nevertheless, as shown in Fig. 27, the SAR analysis demonstrates that the MIMO antenna operates within acceptable safety limits. Overall, the impedance bandwidth encompasses

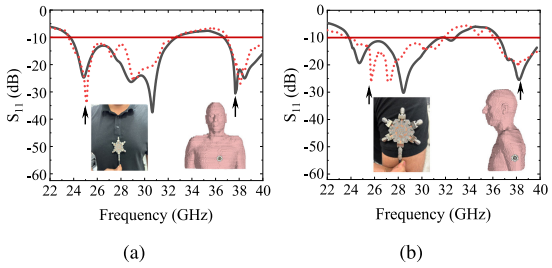

FIGURE 28. Reflection coefficient results on (a) the chest and (b) arm.

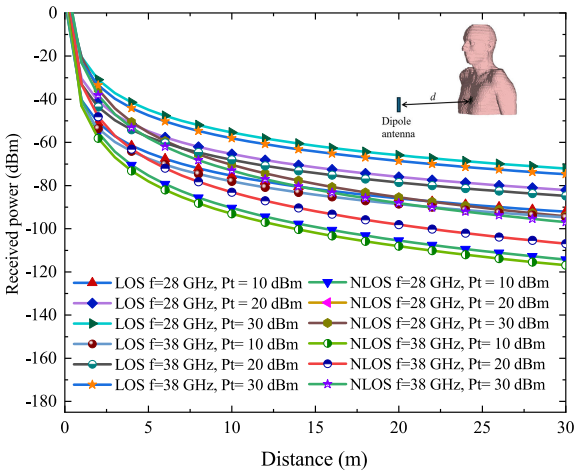

FIGURE 29. Received power by the dipole antennain LOS and NLOS conditions.

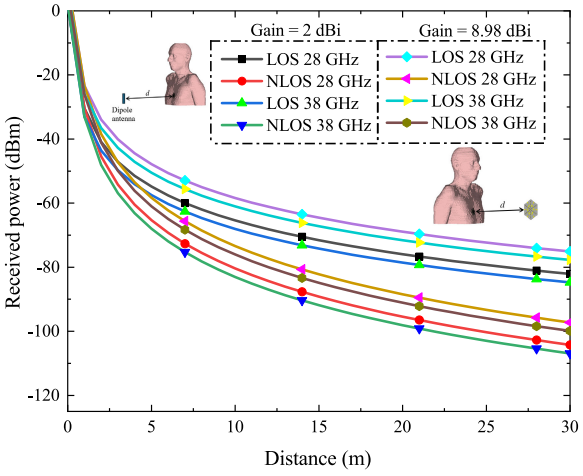

FIGURE 30. Comparison of the received power by the dipole and proposed antenna at a transmitter power of 20 dBm.

the required dual-band, ensuring that the proposed MIMO antenna remains suitable for wearable applications.

B. COMMUNICATION LINK

To assess the communication capacity of the proposed MIMO antenna, link calculations were performed for two scenarios

at the resonant frequencies of 28 GHz and 38 GHz. Evaluating the communication capacity is crucial for ensuring reliable performance in WBAN applications.

Case 1: The MIMO antenna is placed on the chest and operates as a transmitter (Tx), while the ideal $\lambda_o/2$ long dipole antenna functions as a receiver (Rx) situated in free space at a distance (d) from the Tx. The received power P_r is calculated using equations (14)-(15) [47].

$$P_r(\text{dBm}) = P_t(\text{dBm}) + G_t(\text{dB}) + G_r(\text{dB}) - \text{PL}_{dB}(\text{dB}) \tag{14}$$

$$\text{PL}_{dB}(d) = 10n\log_{10}\left(\frac{d}{d_0}\right) + 20\log_{10}\left(\frac{4\pi d}{\lambda_0}\right) + X_\sigma \tag{15}$$

Where P_t represents the transmit power, G_t denotes the transmitter antenna gain, G_r is the receiver antenna gain, and n represents the path loss exponent, which varies depending on whether the communication is line-of-sight (LOS) or non-line-of-sight (NLOS). Additionally, d refers to the distance between the transmitter and receiver antennas, and X_σ represents the shadowing effect, modeled as a Gaussian distribution with a standard deviation. In this study, P_t was set to 10 dBm, 20 dBm, and 30 dBm, while G_r was fixed at 2 dBi to simplify the analysis of the communication link. The transmitter gain G_t was set to 8.98 dBi, which is the average of the measured gains at 28 GHz (9.12 dBi) and 38 GHz (8.77 dBi). The path loss exponent n was set to 1.5 for LOS and 3 for NLOS communication. Theoretically, the ideal value for LOS in free space is 1, while in practical LOS scenarios with minimal obstructions, n can range from 1.5 to 2.5. For NLOS conditions, the path loss exponent typically varies from 3 to 6, depending on the environment and the level of obstruction. In this study, the proposed MIMO antenna was analyzed for distances of up to 30 meters. To reflect realistic propagation conditions, average values of n=1.5 for LOS and n=3 for NLOS were chosen. These values are consistent with empirical studies and widely accepted models for mmWave propagation, particularly in environments with moderate obstructions. The shadowing effect (X_σ) was set to 0 dBm, and the reference distance d_0 was maintained at 1.0 m. The distance was varied up to 30 m, and the MATLAB-simulated results of these conditions are shown in Fig. 29. It was observed that the MIMO antenna, when operating at a high transmit power of 30 dBm, enables the dipole antenna with a 2 dBi gain to receive more than -60 dBm of power at distances of up to 15 m for both LOS and NLOS links at 28 GHz and 38 GHz. Even at a lower transmit power of 10 dBm, the dipole antenna can still receive power greater than -75 dBm at distances of up to 15 m for LOS links at 28 GHz. However, the received power is significantly reduced at 38 GHz for a 10 dBm input power in both LOS and NLOS links, which can be attributed to the higher path losses at this frequency.

Case 2: To evaluate the efficacy of the proposed MIMO antenna in comparison to a dipole antenna, the proposed MIMO antenna was utilized as both the transmitter (Tx) and receiver (Rx) antennas. All parameters from Case 1 were kept constant, except for the gain, where G_r was replaced with G_t (8.98 dBi). The received power was then calculated using Equations 14 and 15. The results for this configuration, with a transmit power P_t of 20 dBm, were compared to those obtained using a dipole antenna with the same P_t of 20 dBm. The received power of this case is shown in Fig. 30. An improvement of 7 dBm in received power was observed at distances beyond 5 meters. This demonstrates

TABLE 3. Link budget parameters.

Transmitter conditions	
Parameter	**Value**
Operating frequency, f (GHz)	28/38
Transmitted power, P_t (dBm)	20
Transmitter antenna gain, G_t (dBi)	9.12/8.77
EIRP ($P_t + G_t$) (dBm)	26.12/25.77
Propagation environment conditions	
Distance, d (m)	0-100
Free space loss, L_f (dB)	Adaptive (distance)
Receiver conditions	
Receiver antenna gain, G_r (dBi)	8.98 (average)
Ambient temperature, T_0 (K)	293
Boltzmann constant, k	1.38×10^{-23} W/m K
Noise power density, N_0 (dB/Hz)	-203.9
Signal conditions	
Bit rate, B_r (Mb/s)	1, 10, 50, 100
Bit error rate	1×10^{-5}
E_b/N_0 (ideal PSK) (dB)	9.6
Coding gain, G_c (dB)	0
Fixing deterioration, G_d (dB)	2.5

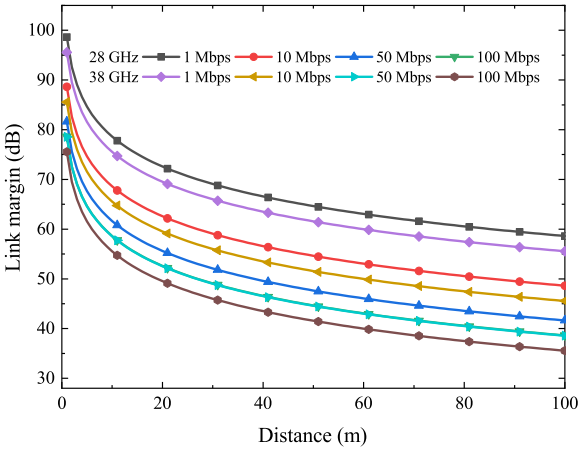

FIGURE 31. LM result of the proposed MIMO antenna.

TABLE 4. Comparison of proposed work with other reported MIMO antennas.

Ref.	Elem.	Size (λ)	B.W (GHz)	Iso. (dB)	Gain (dBi)	ECC	LM (dB)	Decoup. Techn.
[49]	4	1.49×1.12	27.75-28.18/41.31-41.99	>20	6.08/5.78	<0.10	YES	NR
[50]	4	3.61×4.89	26.32–28.84/34–41.5	>15/25	7.4/5.5	0.0001	NR	NR
[51]	6	1.28×2.04	25.1-25.9/37.75-38.6	>20	9/7.2	<0.25	YES	NR
[52]	4	1.79×1.79	26.9-29/34.5-41	>23	9.5	0.0001	NR	Partial ground
[53]	4	1.19×4.70	36.5-39.28	>30	10	3×10^{-5}	NR	Self isolated
[54]	4	0.26×0.26	26-40	>18	6.6	0.001	NR	Disconnected ground
[55]	4	1.65×1.65	27.5-28.50	>20	7.50	0.0025	NR	Self isolated
[56]	8	4.19×4.19	23.30-27.60	>26	8.6	<0.0004	NR	DGS
[57]	4	2.78×1.41	27.5-28.50	>24	7	0.0001	NR	DGS
[58]	4	3.04×4.6	35.18–39.69	>27	8.09	<0.02	NR	NR
Prop.	6	1.97×3.39	23.63-32.90/36.68-40	>33	9.12/8.77	<0.03/0.02	YES	FSS + DGS

Prop.: Proposed, Elem.: number of antenna elemnts λ: lowest frequency of bandwidth, Iso: isolation, NR: not reported.

that employing the same type of antenna at both the Tx and Rx ends can significantly enhance power reception. The received power in both LOS and NLOS scenarios confirms that the proposed MIMO antenna is capable of achieving reliable communication in a WBAN environment.

Link Margin: The link margin (LM) represents the difference between the received signal strength and the minimum required level for reliable communication, ensuring data transmission even in noisy channel environments. It was calculated for the proposed antenna at 28 and 38 GHz using equations (16)-(21), with the link budget parameters provided in Table 3 [48].

$$L.M\ (\text{dB}) = Link\left(\frac{c}{N_0}\right) - Required\left(\frac{c}{N_0}\right) \tag{16}$$

$$Link\left(\frac{c}{N_0}\right) = EIRP - L_f + G_r - N_0\ [\text{dB/Hz}] \tag{17}$$

$$Required\left(\frac{c}{N_0}\right) = \frac{E_b}{N_0} + 10\log_{10}(B_r) - G_c + G_d\ [\text{dB/Hz}] \tag{18}$$

$$L_f = 20\log_{10}\left(\frac{4\pi d}{\lambda}\right)(\text{dB}) \tag{19}$$

$$N_0 = 10\log_{10}(k) + 10\log_{10}(T_i)\ [\text{dB/Hz}] \tag{20}$$

$$T_i = T_0\,(NF - 1)\,[K] \tag{21}$$

The LM of the proposed MIMO antenna for the 20 dBm power case is presented in Fig. 31, showing a decrease in margin as the communication distance increases. At 28 GHz, a higher LM was observed compared to 38 GHz at the same data rate, due to lower path loss at 28 GHz. The LM improves to 55 dB when the separation distance is within 10 meters, which aligns with typical wearable communication ranges. The proposed antenna supports data transmission at 100 Mbps over distances of up to 100 meters for both 28 GHz and 38 GHz, maintaining a link margin above 35 dB. These results confirm that the proposed MIMO antenna can efficiently handle high data rates in the mmWave band offering reliable communication in WBAN.

Table 4 presents a comparison between the proposed $MIMO_3$ antenna and various state-of-the-art MIMO configurations. The proposed MIMO antenna demonstrates superior performance compared to existing designs in the literature [49], [50], [51], [52], [53], [54], [55], [56], [57], and [58]. While [49] achieves moderate isolation (> 20 dB) and gain (6.08 dBi), its operational bandwidth (27.75–28.18 GHz) is significantly narrower than the proposed design's dual-band coverage (23.63–32.90/36.6840 GHz). Similarly, [50] reports excellent ECC (0.0001) but suffers from a larger footprint (3.61λ × 4.89λ). The design in [51] shows comparable gain (9 dBi) but higher ECC (< 0.25) and limited bandwidth (25.1–25.9 GHz). References [53], [54], [55], [56], [57], and [58] exhibit good isolation (> 20 dB) but are constrained by either single-band operation, smaller gain, or lack of reported decoupling methods. The 8-element array in [56] achieves high isolation (> 26 dB) but requires substantially more space (4.19λ × 4.19λ). Compared to these works, the proposed antenna combines the advantages of compact size (1.97λ × 3.39λ), excellent isolation (> 33 dB) through FSS and DGS decoupling, high gain (9.12/8.77 dBi), and low ECC (< 0.03) with additional LM analysis. Due to these characteristics, the proposed MIMO antenna is a promising choice for WBAN and IoT applications in the ISM and mmWave bands.

VII. CONCLUSION

A six-element MIMO antenna designed for mmWave WBAN applications was presented. The design process included CMA analysis at each stage to ensure optimal bandwidth. The proposed MIMO antenna operates across two distinct frequency bands namely 23.63-32.90 GHz covering the ISM band, and 36.68-40 GHz onward covering 5G NR bands. Isolation between the antenna elements was significantly improved through the integration of DGS and FSS, achieving

isolation levels exceeding 33 dB across most of the bandwidth. The antenna exhibits a broadside radiation pattern with realized gains of 9.12 dBi, 9.19 dBi, 8.80 dBi, and 8.77 dBi at 26 GHz, 28 GHz, 30 GHz, and 38 GHz, respectively. The antenna performance was also evaluated on the human body, where minor changes in bandwidth were observed compared with free space operation. Furthermore, the communication link performance, including received power and link margin, is thoroughly investigated. The proposed MIMO antenna's high isolation, dual-band, high gain, and excellent link margin make it promising for WBAN and IoT applications in the ISM and mmWave spectrum.

REFERENCES

[1] A. M. Yacoub, M. O. Khalifa, and D. N. Aloi, "Wide band raised printed monopole for automotive 5G wireless communications," *IEEE Open J. Antennas Propag.*, vol. 3, pp. 502–510, 2022.

[2] A. M. H. Nasr and K. Sarabandi, "A low-cost millimeter-wave 5G V2X multi-beam dual-polarized windshield antenna," *IEEE Open J. Antennas Propag.*, vol. 3, pp. 1313–1323, 2022.

[3] M. Zhumayeva, K. Dautov, M. Hashmi, and G. Nauryzbayev, "Wireless energy and information transfer in WBAN: A comprehensive state-of-the-art review," *Alexandria Eng. J.*, vol. 85, pp. 261–285, Dec. 2023.

[4] M. E. Munir, M. M. Nasralla, and H. Farman, "Design and development of super-compact millimeter wave antenna for future 5G vehicular applications," in *Proc. IEEE 100th Veh. Technol. Conf. (VTC-Fall)*, Oct. 2024, pp. 1–8.

[5] Y.-F. Tsao, A. Desai, and H.-T. Hsu, "Dual-band and dual-polarization CPW fed MIMO antenna for fifth-generation mobile communications technology at 28 and 38 GHz," *IEEE Access*, vol. 10, pp. 46853–46863, 2022.

[6] W. Wang, Z. Fang, K. Tang, X. Wang, Z. Shu, Z. Zhao, and Y. Zheng, "Wideband gain enhancement of MIMO antenna and its application in FMCW radar sensor integrated with CMOS-based transceiver chip for human respiratory monitoring," *IEEE Trans. Antennas Propag.*, vol. 71, no. 1, pp. 318–329, Jan. 2023.

[7] A. S. Md. Sayem, A. Lalbakhsh, K. P. Esselle, J. L. Buckley, B. O'Flynn, and R. B. V. B. Simorangkir, "Flexible transparent antennas: Advancements, challenges, and prospects," *IEEE Open J. Antennas Propag.*, vol. 3, pp. 1109–1133, 2022.

[8] K. Dautov, M. Hashmi, G. Nauryzbayev, and N. Nasimuddin, "Recent advancements in defected ground structure-based near-field wireless power transfer systems," *IEEE Access*, vol. 8, pp. 81298–81309, 2020.

[9] S. A. Haydhah, F. Ferrero, L. Lizzi, M. S. Sharawi, and A. Zerguine, "A multifunctional compact pattern reconfigurable antenna with four radiation patterns for sub-GHz IoT applications," *IEEE Open J. Antennas Propag.*, vol. 2, pp. 613–622, 2021.

[10] G. R. MacCartney and T. S. Rappaport, "Millimeter-wave base station diversity for 5G coordinated multipoint (CoMP) applications," *IEEE Trans. Wireless Commun.*, vol. 18, no. 7, pp. 3395–3410, Jul. 2019.

[11] H. S. Abubakar, Z. Zhao, M. E. Munir, W. U. K. Tareen, B. Wang, S. H. Kiani, and T. Ali, "Enhanced smartphone connectivity: Dual-band MIMO antenna with high isolation and low ECC," *Phys. Scripta*, vol. 99, no. 6, Jun. 2024, Art. no. 065524.

[12] M. Shoaib, G. Husnain, N. Sayed, and S. Lim, "Unveiling the 5G frontier: Navigating challenges, applications, and measurements in channel models and implementations," *IEEE Access*, vol. 12, pp. 59533–59560, 2024.

[13] M. J. Shehab, I. Kassem, A. A. Kutty, M. Kucukvar, N. Onat, and T. Khattab, "5G networks towards smart and sustainable cities: A review of recent developments, applications and future perspectives," *IEEE Access*, vol. 10, pp. 2987–3006, 2022.

[14] G. Ancans, V. Bobrovs, A. Ancans, and D. Kalibatiene, "Spectrum considerations for 5G mobile communication systems," *Proc. Comput. Sci.*, vol. 104, pp. 509–516, Jan. 2017.

[15] P. P. Shome, T. Khan, A. A. Kishk, and Y. M. M. Antar, "Quad-element MIMO antenna system using half-cut miniaturized UWB antenna for IoT-based smart home digital entertainment network," *IEEE Internet Things J.*, vol. 10, no. 20, pp. 17964–17976, Oct. 2023.

[16] S. Zeadally and O. Bello, "Harnessing the power of Internet of Things based connectivity to improve healthcare," *Internet Things*, vol. 14, Jun. 2021, Art. no. 100074.

[17] K. Sultan, M. Ikram, and N. Nguyen-Trong, "A multiband multibeam antenna for sub-6 GHz and mm-wave 5G applications," *IEEE Antennas Wireless Propag. Lett.*, vol. 21, pp. 1278–1282, 2022.

[18] Z. Wang, J. Zhang, H. Du, W. E. I. Sha, B. Ai, D. Niyato, and M. Debbah, "Extremely large-scale MIMO: Fundamentals, challenges, solutions, and future directions," *IEEE Wireless Commun.*, vol. 31, no. 3, pp. 117–124, Jun. 2024.

[19] Y. Da, X. Chen, and A. A. Kishk, "In-band mutual coupling suppression in dual-band shared-aperture base station arrays using dielectric block loading," *IEEE Trans. Antennas Propag.*, vol. 70, no. 10, pp. 9270–9281, Oct. 2022.

[20] U. Qureshi, M. U. Khan, M. S. Sharawi, S. N. Burokur, and R. Mittra, "A graded index all-dielectric lens for field decorrelation and decoupling of a wideband MIMO antenna," *IEEE Open J. Antennas Propag.*, vol. 4, pp. 180–195, 2023.

[21] X. Chen, P. Wang, Y. Shao, and H. Jin, "Gradient relative permittivity superstrate for decoupling of two closely located dual-polarized slot antennas," *IEEE Trans. Antennas Propag.*, vol. 70, no. 4, pp. 3046–3051, Apr. 2022.

[22] Y. Li, L.-A. Bian, K.-D. Xu, Y. Liu, Y. Wang, R. Chen, and S. Xie, "Mutual coupling reduction for monopole MIMO antenna using l-shaped stubs, defective ground and chip resistors," *AEU-Int. J. Electron. Commun.*, vol. 160, Feb. 2023, Art. no. 154524.

[23] H.-H. Tran, T. T. Nguyen, H.-N. Ta, and D.-P. Pham, "Coupling reduction of extremely closely spaced circularly polarized MIMO patch antenna by phase shift method," *IEEE Access*, vol. 11, pp. 65347–65353, 2023.

[24] N. P. Kulkarni, N. Bhaskarrao Bahadure, P. D. Patil, and J. S. Kulkarni, "Flexible interconnected 4-port MIMO antenna for sub-6 GHz 5G and X band applications," *AEU-Int. J. Electron. Commun.*, vol. 152, Jul. 2022, Art. no. 154243.

[25] K. E. Kedze, W. Zhou, N. Javanbakht, G. Xiao, E. Almajali, J. S. Wight, J. Shaker, and R. E. Amaya, "Application of metamaterial wall for mutual coupling mitigation of a dual differential fed 2×2 patch array antenna," *IEEE Access*, vol. 12, pp. 151251–151260, 2024.

[26] L. Ma, Z. Shao, J. Lai, C. Gu, and J. Mao, "A compact dual-decoupling scheme for aperture-coupled and probe-fed closely spaced wideband microstrip antennas," *IEEE Trans. Antennas Propag.*, vol. 71, no. 11, pp. 9072–9077, Nov. 2023.

[27] M. Hussain, W. A. Awan, E. M. Ali, M. S. Alzaidi, M. Alsharef, D. H. Elkamchouchi, A. Alzahrani, and M. Fathy Abo Sree, "Isolation improvement of parasitic element-loaded dual-band MIMO antenna for mm-wave applications," *Micromachines*, vol. 13, no. 11, p. 1918, Nov. 2022.

[28] M. M. Hasan, M. T. Islam, T. Alam, A. Alzamil, and M. S. Soliman, "Electromagnetic coupling shielding in compact MIMO antenna using symmetric T-shaped metamaterial structure for 5G communications," *Opt. Laser Technol.*, vol. 169, Feb. 2024, Art. no. 110046.

[29] Q. Xuan Lai, Z. L. Hu, and Y. M. Pan, "A simple decoupling method for wideband millimeter-wave MIMO magnetoelectric dipole antenna array using parasitic stubs," *IEEE Trans. Antennas Propag.*, vol. 72, no. 10, pp. 7470–7479, Oct. 2024.

[30] Y.-M. Zhang, M. Yao, and S. Zhang, "Wideband decoupled millimeter-wave antenna array for massive MIMO systems," *IEEE Antennas Wireless Propag. Lett.*, vol. 22, pp. 2680–2684, 2023.

[31] W. Song, X.-W. Zhu, L. Wang, and W. Hong, "Simple structure E-plane decoupled millimeter wave antenna based on current cancellation model," *IEEE Trans. Antennas Propag.*, vol. 70, no. 10, pp. 9871–9876, Oct. 2022.

[32] G. Gao, R.-F. Zhang, W.-F. Geng, H.-J. Meng, and B. Hu, "Characteristic mode analysis of a nonuniform metasurface antenna for wearable applications," *IEEE Antennas Wireless Propag. Lett.*, vol. 19, pp. 1355–1359, 2020.

[33] B. G. P. Shariff, S. Pathan, P. R. Mane, and T. Ali, "Characteristic mode analysis based highly flexible antenna for millimeter wave wireless applications," *J. Infr., Millim., THz Waves*, vol. 45, nos. 1–2, pp. 1–26, Dec. 2023.

[34] M. Sharma, T. Addepalli, R. Manda, T. Vidyavathi, and P. R. Kapula, "A detailed insight of 2 × 2 high isolation wideband dual notched band MIMO antenna with evolution initiated by theory of characteristics mode," *Int. J. Microw. Wireless Technol.*, vol. 2023, pp. 1–20, Feb. 2023.

[35] A. Goldsmith, *Wireless Communications*. Cambridge, U.K.: Cambridge Univ. Press, 2005.
[36] G. Ram, "A generalized array factor for time-modulated hexagonal based antenna array geometry with novel trapezoidal switching," *IEEE/CAA J. Autom. Sinica*, vol. 11, no. 9, pp. 1967–1972, Sep. 2024.
[37] K. R. Mahmoud, M. El-Adawy, S. M. M. Ibrahem, R. Bansal, and S. H. Zainud-Deen, "A comparison between circular and hexagonal array geometries for smart antenna systems using particle swarm optimization algorithm," *Prog. Electromagn. Res.*, vol. 72, pp. 75–90, 2007.
[38] Z. Szabó, G.-H. Park, R. Hedge, and E.-P. Li, "A unique extraction of metamaterial parameters based on Kramers–Kronig relationship," *IEEE Trans. Microw. Theory Techn.*, vol. 58, no. 10, pp. 2646–2653, Oct. 2010.
[39] G. E. Evans, *Antenna Measurement Techniques*. Norwood, MA, USA: Artech House, 1990.
[40] M. Manteghi and Y. Rahmat-Samii, "Multiport characteristics of a wide-band cavity backed annular patch antenna for multipolarization operations," *IEEE Trans. Antennas Propag.*, vol. 53, no. 1, pp. 466–474, Jan. 2005.
[41] M. S. Sharawi, "Current misuses and future prospects for printed multiple-input, multiple-output antenna systems [wireless corner]," *IEEE Antennas Propag. Mag.*, vol. 59, no. 2, pp. 162–170, Apr. 2017.
[42] M. P. Karaboikis, V. C. Papamichael, G. F. Tsachtsiris, C. F. Soras, and V. T. Makios, "Integrating compact printed antennas onto small diversity/MIMO terminals," *IEEE Trans. Antennas Propag.*, vol. 56, no. 7, pp. 2067–2078, Jul. 2008.
[43] W. Li, K. W. Leung, and N. Yang, "Omnidirectional dielectric resonator antenna with a planar feed for circular polarization diversity design," *IEEE Trans. Antennas Propag.*, vol. 66, no. 3, pp. 1189–1197, Mar. 2018.
[44] J. Ahmad, M. Hashmi, A. Bakytbekov, and F. Falcone, "Design and analysis of a low profile millimeter-wave band Vivaldi MIMO antenna for wearable WBAN applications," *IEEE Access*, vol. 12, pp. 70420–70433, 2024.
[45] *IEEE Standard for Safety Levels With Respect to Human Exposure to Radio Frequency Electromagnetic Fields, 3 KHz to 300 GHz*, IEEE Standard C95.1-2019, Oct. 2019.
[46] P. Hasgall. (Feb. 2022). *IT'IS Database for Thermal and Electro-Magnetic Parameters of Biological Tissues, Version 4.1*. [Online]. Available: https://itis.swiss/virtual-population/tissue-properties/database/tissue-frequency-chart/
[47] M. K. Elmezughi and T. J. Afullo, "An efficient approach of improving path loss models for future mobile networks in enclosed indoor environments," *IEEE Access*, vol. 9, pp. 110332–110345, 2021.
[48] R. N. Tiwari, V. Kaim, P. Singh, T. Khan, and B. K. Kanaujia, "Semi-flexible diversified circularly polarized millimeter-wave MIMO antenna for wearable biotechnologies," *IEEE Trans. Antennas Propag.*, vol. 71, no. 5, pp. 3968–3982, May 2023.
[49] R. N. Tiwari, D. Sharma, P. Singh, and P. Kumar, "Design of dual-band 4-port flexible MIMO antenna for mm-wave technologies and wearable electronics," *IEEE Access*, vol. 12, pp. 96649–96659, 2024.
[50] W. T. Sethi, S. H. Kiani, M. E. Munir, D. A. Sehrai, H. Savci, and D. Awan, "Pattern diversity based four-element dual-band MIMO patch antenna for 5G mmWave communication networks," *J. Infr., Millim., THz Waves*, vol. 45, nos. 5–6, pp. 521–537, May 2024.
[51] B. G. P. Shariff, T. Ali, P. Kumar, S. Pathan, G. D. G. Simha, P. R. Mane, M. G. N. Alsath, and A.-A.-A. Boulogeorgos, "Dual-band compact six-element millimeter wave MIMO antenna: Design, characterization, and its application for V2V communication," *IEEE Access*, vol. 12, pp. 97951–97968, 2024.
[52] N. Sghaier, A. Belkadi, I. B. Hassine, L. Latrach, and A. Gharsallah, "Millimeter-wave dual-band MIMO antennas for 5G wireless applications," *J. Infr., Millim., THz Waves*, vol. 44, nos. 3–4, pp. 297–312, Apr. 2023.
[53] A. K. Singh and S. Pal, "Compact self-isolated extremely low ECC folded-SIW-based slot MIMO antenna for 5G application," *IEEE Antennas Wireless Propag. Lett.*, vol. 23, pp. 194–198, 2024.
[54] M. E. Munir, M. M. Nasralla, and M. A. Esmail, "Four port tri-circular ring MIMO antenna with wide-band characteristics for future 5G and mmWave applications," *Heliyon*, vol. 10, no. 8, Apr. 2024, Art. no. e28714.
[55] J. Ahmad and M. Hashmi, "A compact MIMO antenna for WBAN applications at millimeter-wave frequencies," in *Proc. 31st Telecommun. Forum (TELFOR)*, Nov. 2023, pp. 1–4.
[56] M. Irshad Khan, S. Liu, M. Kabir Khan, and S. Ur Rahman, "Eight elements mm-wave MIMO antenna for anti-collision radar sensing application with novel hybrid techniques," *AEU - Int. J. Electron. Commun.*, vol. 167, Jul. 2023, Art. no. 154687.
[57] A. E. Farahat, K. F. A. Hussein, and R. R. Elsharkawy, "28 GHz circular polarized MIMO antenna system with polarization diversity for millimeter-wave applications," *Microw. Opt. Technol. Lett.*, vol. 67, no. 2, pp. 1–8, Feb. 2025.
[58] M. A. Haque, M. S. Ahammed, S. Socheatra, R. A. Ananta, M. J. H. Nirob, N. S. S. Singh, N. M. Jizat, S. Alsowail, and S. S. Al-Bawri, "Machine learning based compact MIMO antenna array for 38 GHz millimeter wave application with robust isolation and high efficiency performance," *Results Eng.*, vol. 25, Mar. 2025, Art. no. 104006.

JAWAD AHMAD (Graduate Student Member, IEEE) received the B.S. and M.S. degrees in electronics and electrical engineering from International Islamic University (IIU), Islamabad, Pakistan, in 2017 and 2020, respectively. He is currently pursuing the Ph.D. degree in electrical engineering with the Department of Electrical and Computer Engineering, Nazarbayev University, Astana, Kazakhstan. His research interests include the development of 5G antenna designs, antenna arrays, MIMO antennas, and metamaterial-inspired wearable antennas for biomedical applications.

MOHAMMAD HASHMI (Senior Member, IEEE) received the B.Tech. degree from Aligarh Muslim University, India, the M.S. degree from Darmstadt University of Technology, Germany, and the Ph.D. degree from Cardiff University, Cardiff, U.K. He had held research, engineering, and academic positions with the University of Calgary, Canada; Cardiff University; Thales Electronics GmbH, Germany; Philips Technology Center, Germany; and IIIT Delhi, India. He is currently an Associate Professor with Nazarbayev University, Kazakhstan. His research activities have led to one book, three U.S. patents (two pending), and over 300 journals and conference publications. His current research interests include the domain of advanced RF circuits for wireless applications (including wireless power transfer and energy harvesting), emerging RF circuits and applications, broadband linear and efficient power amplifiers for mobile and satellite applications, and high- and low-frequency instrumentation. He is an Associate Editor of *IEEE Microwave Magazine*.